Nanomaterials and Energy
Volume 1 Issue NME2

Combined positron-annihilation and structural studies of hydrothermally grown zirconia
Fidelus *et al.*

ice | science

Pages 97–106 http://dx.doi.org/10.1680/nme.11.00014
Themed Issue Paper
Received 15/11/2011 Accepted 21/12/2011
Published online 10/01/2012
Keywords: solid oxide fuel cell/oxygen sensor and defects.

ice Institution of Civil Engineers publishing

Combined positron-annihilation and structural studies of hydrothermally grown zirconia

Janusz D. Fidelus
Institute of High Pressure Physics, Polish Academy of Sciences, Warsaw, Poland

Andrzej Karbowski
Nicolaus Copernicus University (UMK), Toruń, Poland

Sebastiano Mariazzi
Dipartimento di Fisica, Università di Trento and INFN, Gruppo Collegato di Trento, Trento, Italy

Ewa Werner-Malento
Institute of Physics, Polish Academy of Sciences, Warsaw, Poland

Roberto S. Brusa
Dipartimento di Fisica, Università di Trento and INFN, Gruppo Collegato di Trento, Trento, Italy

Wuzong Zhou
School of Chemistry, University of St Andrews, Scotland, United Kingdom

Grzegorz P. Karwasz
Nicolaus Copernicus University (UMK), Toruń, Poland

Nanoporous zirconia is used in gas sensors and as a membrane in high-temperature fuel cells. In the present work, positron annihilation spectroscopy and transmission electron microscopy (TEM) were performed on pure zirconia-sintered nanopowders, to determine the porosity. The ortho-positronium annihilation parameter R of zirconia samples, treated at 800°C and 700°C and annealed in oxygen–nitrogen atmosphere with different O_2 contents, were obtained. The photoluminescence, positron annihilation spectroscopy, and TEM studies show presence of defects in all samples. Furthermore, the positron annihilation studies indicate a presence of large free volumes (of the order of few atomic units, at least), open towards the nanocrystals surface what was confirmed by TEM observations which detected a few types of defects such as voids within ≈2–4 interplane distances, stacking faults, terraces and point defects.

1. Introduction

Cubic zirconia (ZrO_2) finds numerous practical applications from jewellery to dentistic ceramics. This pure, wide band gap semiconductor exists in three polymorphic phases at ambient pressure: monoclinic (Smith and Newkirk, 1965; M), tetragonal (Teufer, 1962; T), and cubic (Wyckoff, 1963; C) at high temperatures (above 2370°C where the T–C transition occur). The M–T transformation is observed at 1170°C, and below this temperature the material transforms to the M phase, which is thermodynamically stable (Subbarao, 1981). The essential structural differences between mentioned zirconia phases are due to displacements of the oxygen atoms within the lattice (Cabello *et al.*, 2008). Cubic (or tetragonal) zirconia is usually stabilized by using specific additives (for a review, see, Evans and Cannon, 1986). Stabilization of technological important high symmetry T or C phases at ambient conditions (i.e. by doping with trivalent cations) leads to formation of oxygen vacancies which are responsible for the stabilization of the phases (Fabris *et al.*, 2002) as well as have an effect on properties of the material. Nowadays, thanks to its high oxygen-ion conductivity, this material finds applications in high-temperature solid oxide fuel cells (SOFC) membranes in which the diffusion of the O^{2-} through a zirconia-based electrolyte takes place (Lloyd, 1999). However, monoclinic ZrO_2 is also of great interest as a support material in a variety of catalyst systems (Mercera *et al.*, 1990) and more recently as a material for optical oxygen sensor (Fidelus *et al.*, 2007, 2009; Łojkowski *et al.*, 2005; Smits *et al.*, 2011). Such applications require materials with nanosize particles, possess large surface area, unusual adsorptive properties, surface defects, good thermal and chemical stabilities, as well as fast diffusivities (Gesser and Goswami, 1989; Pajonk, 1991). For these reasons, the nanosynthesis is still a hot topic for industry as indicated by hundreds of millions dollar funding all over the globe (For US, read *American Ceramic Society Bulletin*, 2006).

There are various synthesis techniques of nanosize zirconia (Gole *et al.*, 2006; McCormick *et al.*, 2001). Among them, a low-temperature and environmentally safe hydrothermal route is one of the most extensively employed (Sõmiya and Akiba, 1999; Subbarao, 1981). Microwave-hydrothermal method was established in 1992 by Roy and Komarneni (1992) and is continuously developed. The parameters of precipitation, the methods of preparation, and the doping ions are all factors having a substantial impact on the final crystal phase of zirconia. The combination of microwave (MW) and hydrothermal techniques gives such benefits like a fast heating of the reactions in comparison to conventional method, phase

homogeneity, controlled particle morphology and high purity conditions (Byrappa and Adschiri, 2007). Presently, microwave high-pressure (MW&HP) reactors are developed due to the usefulness for reactions carried out under elevated pressures and energy saving. The MW&HP synergy gives short heating times (because of delivering high microwave power density to fluids under pressure without contact to heater elements) leading to weakly agglomerated nanoparticles, with high crystallinity and narrow grain-size distribution (Blythe *et al*., 2004; Leonelli and Lojkowski, 2007). In hydrothermally microwave-grown zirconia, the stoichiometric ratio of O to Zr can vary and the material shows extended nanoporosity. Therefore, it creates an opportunity for proper applications as high-temperature sensor of oxygen in exhaust gases (Ivers-Tiffe *et al*., 2001), optical oxygen sensor (Fidelus *et al*., 2007), and as high-temperature membrane in fuel cells (Fergus, 2006). It is known that the properties of pure and doped nanosize particles are critically dependent on morphology (the defect concentration, the degree of crystallinity, the shape and size) and the nature, amount, and distribution of dopants (Armelao *et al*., 2008). Due to surface energy effects in nanomaterials, oxygen vacancies may be stabilized in undoped isolated nanoparticles of less than 10 nm diameter and in aggregated nanoparticles of less than 33 nm diameter (Shukla and Seal, 2007). Complementary, TEM, and positron nondestructive techniques permit to analyze the existence and morphology of meso and nanopores (Brusa *et al*., 2004; Zhou *et al*., 1998), presence of defects (see Procházka *et al*., 2008; Yang *et al*., 2010) in the crystalline structure and to understand the detailed formation mechanisms (Evans and Cannon, 1986) and the chemical surroundings of defects (Brusa *et al*., 2001). Combined experimental techniques applied to ZrO_2 nanostructured material should facilitate obtaining samples being a thermodynamic compromise between the following: (a) the crystallographic composition (M–T), (b) defected or defect-free (oxygen vacancies against other defects) structure, (c) the level of sintering against the nanoporosity—constant or variable in depth.

Positron annihilation spectroscopies, (see, for example, Karwasz *et al*., 2004), allow identification of vacancy-like defects, that is, vacancies, clusters of vacancies, nanovoids, stacking faults (but not interstitials) at concentrations less than 1 ppm. If a positron beam facility with controlled injection energies is used, scanning in depth can be done with the resolution of tens of nanometers. An injected positron may (a) annihilate with electrons of the bulk, (b) be trapped into defects what results in its longer lifetimes and a narrower 2-γ annihilation line, or (c) exit into free volumes (pores, nanovoids) to form positronium, giving (in the ortho-Ps state) very long-lifetime component (up to 142 ns) and a 3-γ annihilation signal. Various complementary positron-based techniques should be used in search of specific material features. Doppler broadening of the 2-γ line with the use of a positron beam is a versatile technique for depth scanning in search of defects; however, the interpretation of results needs some reference (possibly defect-free) samples, see, for example, Reference (Brusa *et al*., 2001). Theoretical predictions in this field are not easy. The theory is quite successful in predicting the lifetimes in bulk and in defects, proving also the electric charge of defects, but lifetime measurements resolved in depth are a challenging task and their time-resolution is still limited to about 270–300 ps (Zecca and Karwasz, 2001). Lifetime measurements in bulk material show better time resolution, down to 180 ps (Karbowski *et al*., 2011), but perform averaging over the sample depth. As a substitute for depth-resolved lifetime measurements, the positron beam for Doppler-broadening can be used to trace nanovoids by monitoring t he 3-γ signal (Brusa *et al*., 2004).

Previous studies of zirconia with the lifetime (bulk) techniques were performed mostly for fully stabilized ZrO_2:Y samples (Procházka *et al*., 2008). Recent data for a three-component zirconia, ZrO_2:Y_2O_3 (3% mol.):Cr_2O_3 (0–5% mol.), for possible catalytic applications, showed presence up to four lifetimes, from about 180 ps to 1·5–30 ns (Procházka *et al*., 2011). The two long-lifetime components disappear in samples containing Cr_2O_3 and only two components are present, namely τ_1=180–260 ps and τ_2=380–400 ps.

In this paper, the morphology and structural data acquired by combined positron-annihilation and transmission electron microscopy (TEM) studies for hydrothermally grown zirconia are presented and compared to previous positron studies for similar samples.

2. Experimental

2.1 Samples

Nanoscaled samples were prepared from zirconia nanopowders obtained in hydrothermal microwave-driven process followed by annealing up to 900°C, and then annealed under variable oxygen pressure. The precursor solution was zirconium (IV) oxide chloride octahydrate ($ZrOCl*8H_2O$) min. 99·5% purity (Riedel-de Haen, Germany) into distilled water, with pH of 10, adjusted by adding 1 M NaOH. The syntheses were performed in MW&HP ERTEC reactor (Wrocław, Poland) under a pressure of 6 MPa (accuracy–0·5 MPa) at 280°C (calculated from p/T diagram for water) for 30 min (20 min heating, 10 min cooling). Such conditions correspond with a delivered power density in the range 4–5 W/ml—much less in comparison to conventional reactors. The detailed experimental procedure is described elsewhere (Fidelus *et al*., 2010). Pellets of 1 cm in diameter and 1 mm in thickness were formed under a 130 MPa and 460 MPa pressure. The thermal treatment (at 700°C–900°C) enables us to obtain particles stable at 340°C, that is, at the temperature at which the samples were annealed under different oxygen pressure. The ZrO_2 samples were loaded into quartz tube from which the air was evacuated. The tube was filled with mixtures of oxygen and nitrogen having total pressure of 1000 mbar. The oxygen partial pressure was variable from 21 mbar up to 26 mbar. Additionally, the samples were tested in vacuum (10^{-4} mbar). The individual stages of material treatment are described in details in a previous report (Fidelus *et al*., 2007).

2.2 Characterization

The ZrO_2 samples were characterized by x-ray diffraction (XRD) using a Philips X'pert MPD ALPHA1 PRO diffractometer operating at 40 kV and 30 mA with Cu $K_{\alpha 1}$ radiation, equipped with a primary-beam Johansson Ge monochromator and a strip detector. Data were collected in a continuous mode, and recorded with a step length of 0·0167 in the angular region of 2θ from 5° to 159°. Rietveld method performed with FullProf2k program (Rodriguez-Carvajal, 1994) was used for quantitative phase analysis and structure refinement.

The density of the annealed nanopowders was measured by means of helium picnometry using a AccuPyc 1330, produced by Micrometrics Instruments.

The specific surface-area analysis was determined by the multipoint B.E.T. method (Gemini 2360, Micromeritics Instruments).

Positron measurements have been performed with two techniques: (a) depth-resolved Doppler broadening (Brusa *et al*., 2000, 2004) and (b) the lifetime technique in bulk (Karbowski *et al*., 2011). The ORTEC positron lifetime spectrometer is based on plastic scintillators (St. Gobain BC418) and RCA 8850 photomultipliers. The electronics consisting of two 538B constant fraction discriminators, the 414A fast coincidence module and the 537 time-to-amplitude converter. The lifetime resolution as tested in several types of materials is about 180 ps (Karbowski *et al*., 2011).

The spectrometer uses a ^{22}Na radioactive source (12 μCi) in 7 μm thick kapton sandwich, with one side covered by a stainless steel (AISI 316LN) 1 mm thick plate and with second side by investigated ZrO_2 sample. AISI 316LN stainless steel is an iron-based noncorrosive, nonmagnetic steel with low (0·08%) carbon contents and high chromium and nickel contents (typically 16% and 13%, respectively). The back plate in our radioactive source acts as its mechanical reinforcement and simulates conditions of some background signal present, for example, in beam experiments. In apparatus calibration procedures, in the stainless steel was found a single lifetime component of 146 ps. This was kept as constant, with 50% intensity in all the analysis.

Measurements for each ZrO_2 samples were done in several series, each with 12–48 h acquisition time and $1{\cdot}0–1{\cdot}5 \times 10^6$ counts in spectra. The analysis of lifetime spectra was performed with the LT package by J. Kansy (1996). The LT package is quite flexible and allows to obtain positron lifetime as a sum of single components or as a distribution of components. The source lifetime component was 382 ps (because of the kapton sandwich) and the source contribution 14% of the total annihilation intensity.

Doppler broadening measurements of the 511 keV line were carried out with an electrostatic slow positron beam (Zecca *et al*., 1998) tunable in the 0·05–25 keV energy range, which corresponds to a depth scale of 1 to about 3000 nm, depending on sample density. The machine can operate in a low-energy mode (50 eV to 2 keV) with a beam diameter (FWHM) from 2·9 to 1·7 mm or in a high-energy mode (1 keV to 50 keV) with a FWHM from 1·4 to 1·0 mm. The transverse spot position on the target is very stable, with wandering being much smaller than the beam diameter. The apparatus transmission function is flat, with the intensity change of only 30% when going from 10 eV to 50 keV.

The mean positron implantation depth z is related to the positron implantation energy E through the equation:

$$1. \qquad z = \left(\frac{40}{\rho}\right) E^{1.6}$$

where z is in nanometers, ρ - density is expressed in grams per cubic centimeter and energy E in keV, respectively (Asoka-Kumar *et al*., 1994). The mean density of the nanoporous ZrO_2 samples, 5·6 g/cm^3 was used for the calculation of the positron implantation depth.

The detector consisted in HPGe monocrystal with resolution 1·2 keV at the 511 keV annihilation line. The parameter S was calculated as the ratio of the counts in the central area ($| 511- E_\gamma | \le 0{\cdot}85$ keV) and the total area of the 511 keV peak ($| 511- E_\gamma | \le 4{\cdot}25$ keV). As the central area of the 511 keV peak corresponds to the annihilation mainly with low-momentum electrons, the higher value of the S parameter indicates the absence of ionic cores at the annihilation sites. Therefore, the rise of the S parameters indicates the increasing number of vacancy-like traps in the solid.

The formation of o-Ps has been evaluated through the R-parameter: ratio between the counts in the low-energy valley, $410 \text{ keV} \le E_\gamma \le 500$ keV (i.e. 3γ annihilations), and the counts in the 511 keV peak (2γ annihilations). The scale for the R-parameter was evaluated by measuring the Ps formation in a Ge crystal. The no-formation of Ps (R_0) was evaluated by measuring R at high positron implantation energies, while the 100% Ps formation (R_{100}) was evaluated by extrapolating at zero positron implantation energy R measured with the Ge at 1000 K, see (Brusa *et al*., 2003). The R_n parameter defined as $(R\text{-}R_0)/(R_{1000}\text{-}R_0)$ is the fraction of positrons forming positronium (FPs) times the three-gamma annihilation probability [41]: $R_n = F_{PS}\,\lambda_{3\gamma}/(\lambda_{3\gamma} + \lambda_{p.o.})$, where $\lambda_{3\gamma} = (142{\cdot}1 \text{ ns})^{-1}$ is the o-Ps annihilation rate in vacuum and $\lambda_{p.o.}$ the pick-off annihilation rate which is related to the void-size of the pores (Consolati, 2002). In the following we have applied this equation with $F_{PS} = 100\%$ to estimate the equivalent radius of the nanopores.

The samples for TEM and high-resolution TEM (HRTEM) studies were prepared by dispersing the ZrO_2 powder on a holey carbon film supported on a copper grid, and the images were recorded on

a JEOL JEM-2010HR electron microscope operated at 200 kV and equipped with a Gatan GIF Tridiem system.

3. Results and discussion

Structural properties of zirconia nanocrystals were analyzed by Rietveld refinement. The crystallite size was determined by XRD using the Scherrer equation, and by TEM. The results of Rietveld analysis of XRD patterns for ZrO_2 nanopowder annealed from 700°C –900°C are presented in Figure 1. As one can see, some differences in crystal structure of ZrO_2 nanoparticles annealed at various temperatures can be observed. The XRD pattern show that ZrO_2 is composed of both monoclinic (majority) and tetragonal (minority) phases after annealing at 700ºC. When nanoparticles are further annealed at 800°C and 900°C, the monoclinic phase is stabilized and the tetragonal structure is completely disappeared. The lattice constants for the M and T phases of studied samples are presented in Table 1. The values are in good agreement with those of the reference data (Inorganic, 2009; Ray *et al.*, 2000). The average crystallites size, for all samples, determined by XRD using the Scherrer equation and calculated from selected reflections with 2 theta of about 30°–60° are shown in Table 1. As seen in this Table, the value of lattice parameter *a* does not change within the error while the value of lattice parameters *b* and *c* decreases and increasers, respectively, with increasing annealing temperature. The β angle decreases smoothly with increasing annealing temperature. In further, detailed analysis, the focus was on single-phase ZrO_2 sample annealed at 800°C. The average size of the annealed nanocrystals (M), based on XRD analysis, was 26·3(1) nm. This value is in reasonable agreement with the TEM observation presented in Figure 2. The shape of the particles is quite spherical. The particles are monolithic without any twinnings. The results of specific surface analysis ≈30 m^2/g, are consistent with this grain-size range. High density, ≈5·9 g/cm^3, of nanopowder indicate its good quality with a high degree of crystallinity what is illustrated in Figure 3.

Surface morphology and structure of annealed ZrO_2 have been carried out by TEM. Figure 3 shows HRTEM images of typical particles from specimens after annealing at 800°C and treated in vacuum or in different oxygen partial pressures at 340°C. All the particles are slightly aggregated what is typical for the products of hydrothermal synthesis. These polycrystalline particles show different type of defects. The TEM micrograph of a thin slice of an individual ZrO_2 particle in Figure 3(a) clearly reveals some inhomogeneity—defects randomly distributed within the whole particle. Many voids with 2–3 nm in diameter appeared as white spots indicated by the yellow arrows. The black small spots pointed by the white arrows could be point defects, of unknown type, maybe some nonstechometric ZrO_x complexes. It is assumed that probably, these defects were created by the treatment in vacuum. The point defects seen presently (small black spots) were also detected in our previous work, see the References (Ruiz–Morales *et al.*; 2006; Zhou, 2008). Figure 3(b) shows a different structure of the particles

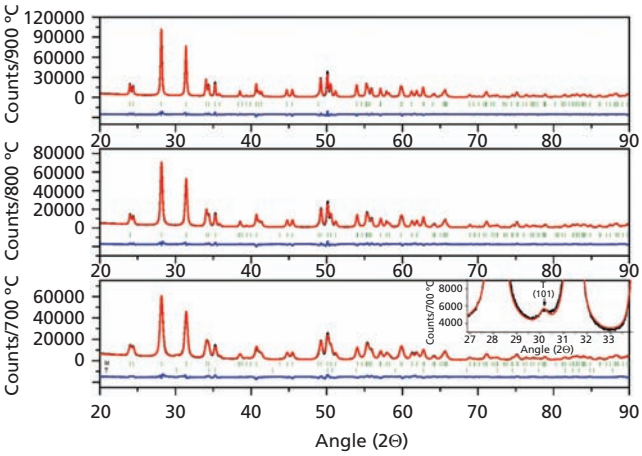

Figure 1. (color on-line) Details of Rietveld refinement plot of the ZrO_2 after annealing at 700, 800 and 900°C. Experimental pattern is formed from crosses and the solid line is the calculated profile; vertical bars labeled M and T show the positions of diffraction peaks of the monoclinic and tetragonal phases, respectively. Difference pattern is shown below the bars. The inset documents the presence of tetragonal phase in the sample annealed at 700°C and the fit quality. The characteristic weak reflection of this phase, 101, is indicated by an arrow.

Sample	ZrO_2-700°C	ZrO_2-800°C	ZrO_2-900°C
	Monoclinic phase (M)		
a [Å]	5.1485 (5)	5.1481 (3)	5.1482 (3)
b [Å]	5.2054 (6)	5.2051 (3)	5.2037 (3)
c [Å]	5.3188 (6)	5.3196 (3)	5.3214 (3)
b	99.206 (7)	99.187 (5)	99.164 (3)
	Tetragonal phase (T)		
a [Å]	3.596 (7)	—	—
c [Å]	5.205 (2)	—	—
	Phases content (weight %) in annealed samples		
M [%]	99 ± 2	100	100
T [%]	1.1 ± 0.3	0	0
	Grain size [nm]		
M [nm]	18.5 (1)	26.3(1)	35.7(1)
T [nm]	10.1 (2)	—	—

Table 1. Phases content (weight %), lattice parameters and the grain size in ZrO_2 samples annealed from 700°C–900°C.

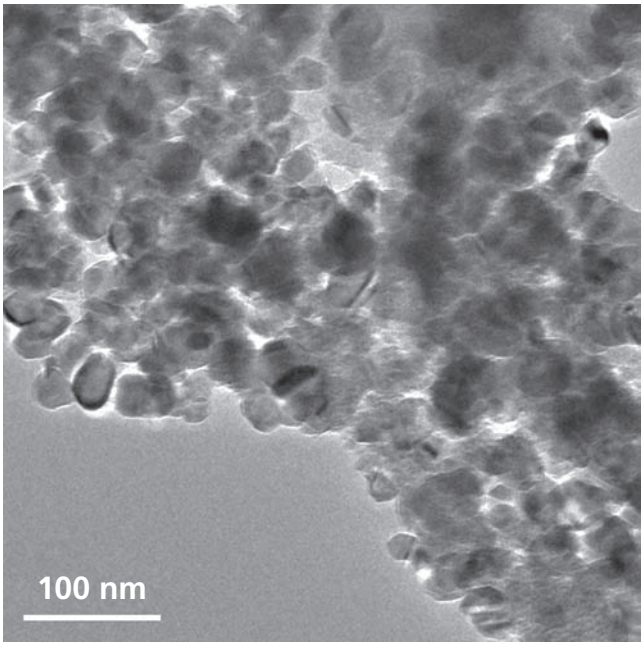

Figure 2. TEM image of the ZrO_2 nanopowder obtained by coprecipitation method followed by a hydrothermal microwave-driven treatment and annealed at 800°C (air atmosphere).

treated in the air or vacuum. Some stacking faults in the particle illustrated by the arrows are visible at micrograph. Furthermore, detailed observations shown that additional type of defects occur in the samples treated under vacuum, mainly: terraces marked by the arrow (see Figure 3(c)).

The analysis of lifetime spectra shows three positron lifetime components, $\tau_1 = 180 \pm 5$ ps, $\tau_2 = 406 \pm 10$ ps and $\tau_3 = 17 \pm 5$ ns (see Table 2). The intensity of the second positron lifetime component is high (84)% for the sample annealed at 700ºC and decreases to 34% with the rise of the annealing temperature to 900ºC. In the same manner, the longest lifetime component falls, from 6·4 % to 2·6 %, for samples annealed at 700ºC and 900ºC, respectively. The quality of the fit as evaluated by the χ^2 parameter is good (below 1·01), see Table 2.

Present lifetime values agree, in general, with measurements (Proházka *et al*., 2008) in pure zirconia powder, in yttrium stabilized powder, in sintered and in crystalline samples. In pure zirconia powder, four lifetime components were found, $\tau_1 = 189$ ps and $\tau_2 = 373$ ps with 45% intensities each and $\tau_3 = 2$ ns and $\tau_4 = 34$ ns with 1·5% and 7·5% intensities, respectively. The long-lifetime components disappeared in samples sintered at 1200ºC/1h (ZrO_2 with 3 mol.% Y_2O_3; Proházka *et al*., 2008). As far as the τ_1 and τ_2 from present and Procházka *et al*. (2008) measurements match each other within our experimental uncertainty, our τ_3 is somewhat shorter.

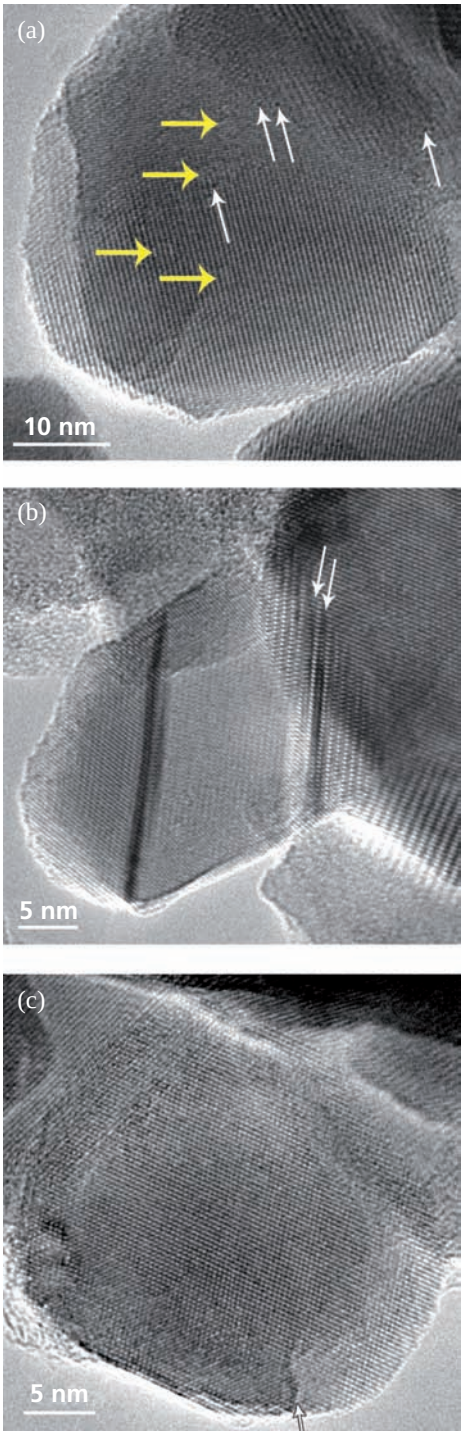

Figure 3. TEM of the ZrO_2 nanopowders treated at 800°C and annealed at 340°C (20 min) in oxygen–nitrogen atmosphere with different O_2 contents: (a) voids with ≈2–3 nm in diameter appeared as white spots indicated by the yellow arrows and some other the point defects appeared as black small spots pointed by the white arrows (vacuum), (b) stacking faults indicated by the arrow marks (air atmosphere or vacuum), (c) terraces illustrated by the arrow (vacuum).

No.	T [°C]	τ_1 [ps]	I_1 [%]	τ_2 [ps]	I_2 [%]	τ_3 [ns]	I_3 [%]	Variance
1	700	180	9.2	405	84.4	19.8	6.4	1.003
2	800	180	31.2	407	65.4	17.0	3.4	1.005
3	900	180	63.0	405	34.4	18.3	2.6	1.004

Table 2. Positron lifetime deconvolution into three components for the ZrO_2 samples pressed under 460 MPa pressure and sintered at the given temperature *T*.

The shortest lifetime observed both in present as well as in zirconia nanopowders by Proházka, *et al*. (2008, 2011) corresponds, probably, to trapping in vacancy-like defects, probably single vacancies. This conclusion is supported by measurements by Proházka *et al*. (2008) for monocrystalline ZrO_2:Y_2O_3, where the $\tau_1 = 189$ ps component present in powder samples is replaced by $\tau = 168$ ps, predicted theoretically for zirconia polymorphs (Proházka *et al*., 2008). In our data, the $\tau_1 = 180$ ps lifetime is found for all samples, indicating that defects inside the nanograins exist also in samples annealed at 900ºC.

The second component is to be attributed to larger defects and/or open volumes comparable to several defects. A rough comparison to our extensive studies of Czochralski-type silicon oversaturated with oxygen (Brusa *et al*., 2001) indicates that these defects are probably larger than few vacancies and are rather nanovoids; however, we are not aware of any theories to compare with. Proházka *et al*. (2008) suggested triple points at grain boundary intersections as possible sites for the annihilation with the $\tau_2 = 371$–383 ps lifetime. In the studied nanograins, the present TEM results visualized extended defects: stacking faults, terraces, voids, and generating vacancies; the lowering of the positron τ_2 lifetime intensity shows that they gradually disappear with the rise of annealing temperature. These defects were attributed rather than grain boundaries to the observed value of τ_2. The lowering of the τ_2 intensity shows that these defects gradually disappear with the rise of the annealing temperature.

The longest lifetime indicates formation of the o-Ps. In our measurements, the $\tau_3 = 17 \pm 5$ ns lifetime is shorter than the value of 34 ns found by Proházka *et al*. (Proházka *et al*., 2008) for nonsintered nanopowders. An exact evaluation of free nanovolumes available for the Ps formation is not easy (Consolati, 2002); the observed τ_3 value indicates the "dimensions" of the free volumes of a few (1–3) nanometers (see the results quoted in Reference (Consolati, 2002)).

Doppler-broadening measurements show *S*-parameter values rising towards the surface, see Figure 4. However, this rise is not significant and should not be related to changes in defects concentrations but rather to the probability of positronium formation (which also gives a rise in the *S*-parameter). A sole conclusion that samples

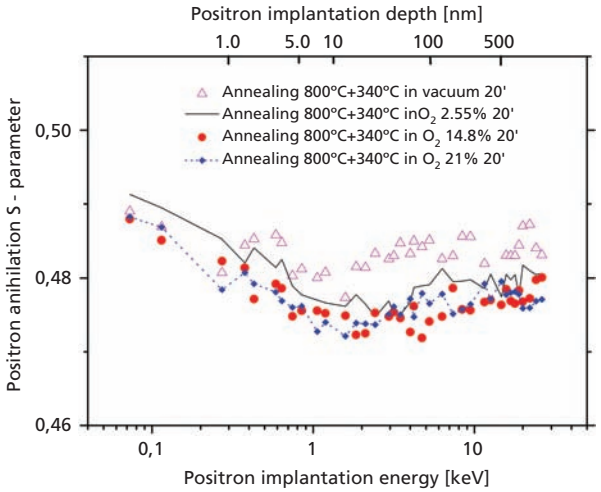

Figure 4. Positron annihilation Doppler broadening *S*—parameter for nanostructured pure zirconia samples, treated at 800ºC and annealed in oxygen–nitrogen atmosphere with different O_2 contents.

are pretty uniform in the whole examined, that is, down to about 1 micrometer depth, is drawn from Figure 4.

The *S*-parameter in bulk lowers after annealing in oxygen atmosphere. This, again, can indicate the varying probability of the Ps formation due to the higher availability of electrons to form Ps on grain surfaces after annealing in oxygen atmosphere (a property which is important in ionic conductivity of ZrO_2). Decisive on existence of Ps inside samples are measurements of the *R*-parameter.

For all samples, the three-gamma annihilation signal is high and rises towards the surface, see Figure 5. The *R*-parameter changes from 10% at 0·5 nm depth to 5% at depths greater than 5 nm. This indicates the presence of relatively large free volumes. Assuming that 100% of positron implanted form Ps (which certainly is not the case), the lower limit on the cavity radii is assumed as 0·6 nm. Beam measurements show that these cavities extend for the whole depth examined, that is, down to about 1 micrometer. Note that such a feature is particularly important in gas-sensor applications.

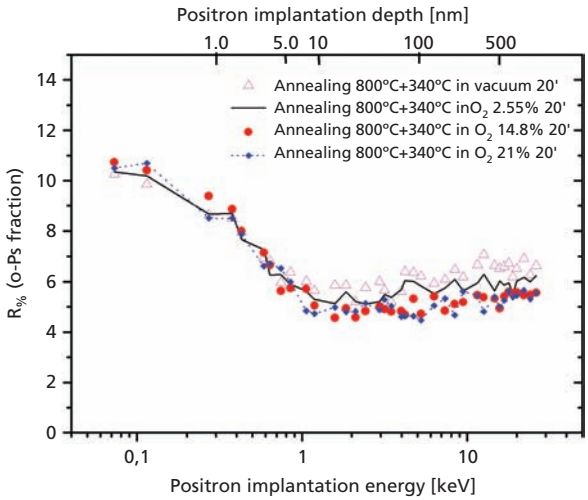

Figure 5. Fraction of ortho-positronium annihilation in nanostructured pure zirconia samples, treated at 800ºC and annealed in oxygen—nitrogen atmosphere with different O_2 contents.

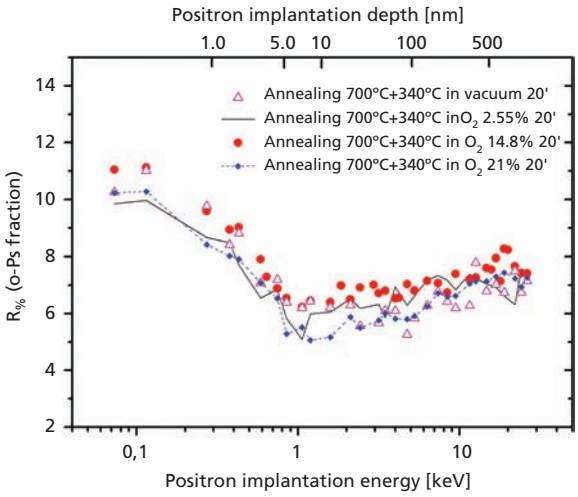

Figure 6. Fraction of ortho-positronium annihilation in nanostructured pure zirconia samples, treated at 700ºC and annealed in oxygen—nitrogen atmosphere with different O_2 contents.

The samples sintered at 700º C (being a mixture of M–T phases) and in particular annealed with higher oxygen contents show a relatively higher Ps fraction in the bulk, see Figure 6. Note however, that the ortho-positronium signal depend not only on the open volumes but also on the surface features (chemical terminations) of the nanograins. In fact, annealing in oxygen-rich atmosphere lowers the o-Ps signal and makes the samples more uniform below 10 nm in depth, see Figure 5. Probably, terminating the surface of nanopores with oxygen atoms and/or saturation of oxygen vacancies changes the probability of o-Ps formation.

4. Conclusions

Nanoscaled zirconia samples were obtained in hydrothermal microwave-driven process followed by annealing up to 900°C, and then annealed under variable oxygen pressure. In beam measurements, a high fraction (8%–11%) of ortho-positronium has been detected, indicating a nanoporous structure within the whole material but particularly down to first 20 nm. The porosity after annealing in oxygen atmosphere is lower in samples annealed at 800ºC than in samples annealed at 700ºC; the difference in annealing temperature does not influence the porosity of surface layers. Also from bulk lifetime measurements, it is deduced on presence of nanopores in all samples annealed in the 700–900ºC temperature range—apart from short (180 ps) lifetime component, probably due to vacancies in the ZrO_2 crystalline phase and an intermediate (about 400 ps) component typical for extended defects, a long-lifetime is noted, indicating formation of positronium in intergrain volumes.

TEM studies for ZrO_2 nanopowder annealed at 800°C confirmed the presence of different defects such as stacking faults, voids within ≈2–4 interplane distances, terraces, and some other point defects. This is a clear hint for further, functional studies of this material as well as of similar systems like YSZ(Pr, Eu) or ZnO(Bi).

Positron studies by both lifetime technique in bulk and the Doppler broadening with a positron beam show that the hydrothermally grown ZrO_2 samples exhibit some significant nanoporosity extending into the depth of several hundreds nm. Annealing at high temperature, and in particular in oxygen atmosphere, changes the crystalline structure and also the porosity, although the persistence of the long-lifetime component shows that the nanopores are still efficiently stabilized. Depth-resolved identification of defects with a pulsed-positron beam (Zecca and Karwasz, 2001) would be desirable.

Acknowledgments

This work was partly supported by grants no. N N508 0851 33 and N N202 1288 39 of Ministry of Science and Higher Education (Poland). The ORTEC positron lifetime system has been purchased within the NLTK laboratories (grant no. POIG 02.02.00-00-003/08) at NCU in Toruń.

REFERENCES

Armelao L, Bottaro G, Pascolini M *et al.* (2008) Structure-luminescence correlations in europium-doped sol-gel ZnO nanopowders. *Journal of Physical Chemistry C* **112:** 4049–4054.

Asoka-Kumar, Lynn KG and Welch DO (1994) Characterization of defects in Si and SiO_2 using positrons. *Journal of Applied Physics* **76:** 4935.

Blythe HJ, Ibrahim RM, Gehring GA, Neal JR, and Fox AM (2004) Mechanical alloying: A route to room-temperature ferromagnetism in bulk Zn1-xMnxO. *Journal of Magnetism and Magnetic Materials* **283**:117–127.

Brusa RS, Karwasz GP, Tiengo N *et al*. (2000) Formation of vacancy clusters and cavities in He-implanted silicon studied by slow-positron annihilation spectroscopy *Physical Review B* **61:** 10154.

Brusa RS, Deng W, Karwasz GP, Zecca A, and Pliszka D (2001) Positron annihilation study of vacancy-like defects related to oxygen precipitates in Czochralski-type Si. *Applied Physics. Letters* **79:**1492–1495.

Brusa RS, Karwasz GP, Mariotto G *et al*. (2003) Structural evolution in Ar+ implanted Si-rich silicon oxide. *Journal of Applied Physics* **94:** 7483–7492.

Brusa RS, Spagolla M, Karwasz GP *et al*. (2004) Porosity in SiOCH films depth profiled by positron annihilation spectroscopy *Journal of Applied Physics* **95**: 2348.

Byrappa K and Adschiri T (2007) Hydrothermal technology for nanotechnology. *Progress in Crystal Growth and Characterization of Materials* **53:**117–166.

Cabello G, Lillo L, Caro C *et al*. (2008) Structure and optical characterization of photochemically prepared ZrO_2 thin films doped with erbium and europium. *Journal of Non-Crystalline Solids* **354:** 3919–3928.

Consolati G (2002) Positronium trapping in small voids: influence of their shape on positron annihilation results. *Journal of Chemical Physics* **117:** 7279–7283.

Evans AG and Cannon RM (1986) Toughening of brittle solids by martensitic transformations. *Acta Metallurgica* **34:** 761–800.

Fabris S, Paxton AT and Finnis MW (2002) *A* stabilization mechanism of zirconia based on oxygen vacancies only. *Acta Metallurgica* **50:** 5171–5178.

Fergus JW (2006) Electrolytes for solid oxide fuel cells. *Journal of Power Sources* **162:** 30–40.

Fidelus JD, Karbowski A, Mariazzi S, Brusa RS and Karwasz G (2010) Positron-annihilation and photoluminescence studies of nanostructured ZrO_2. *Nukleonika* **55:** 85–89.

Fidelus JD, Lojkowski W, Millers D *et al*. (2007) Zirconia based nanomaterials for oxygen sensors—Generation, characterisation and optical properties. *Solid State Phenomena* **128:** 141–150.

Fidelus JD, Lojkowski W, Millers D, Smits K and Grigorjeva L (2009) Advanced nanocrystalline ZrO_2 for optical oxygen sensors *Proceedings of the IEEE Sensors* 2009 art. no. 5398385 1268–1272.

Gesser HD and Goswami PC (1989) Aerogels and related porous materials. *Chemical Reviews* **89:** 765–788.

Gole JL, Prokes SM, Stout JD, Glembocki OJ and Yang R (2006) Unique properties of selectively formed zirconia nanostructures. *Advanced Materials* **18:** 664–667.

Inorganic Crystal Structure Database #172161 (2009) Karlsruhe 2007/04/01.

Ivers-Tiffe E, Hardtl KH, Menesklou W, and Riegel J (2001) Principles of solid state oxygen sensors for lean combustion gas control. *Electrochimica Acta* **47:** 807–814.

Kansy J (1996) Microcomputer program for analysis of positron annihilation lifetime spectra. *Nuclear Instruments and Methods in Physics Research* **374:** 235–244.

Karbowski A, Fidelus JD and Karwasz G (2011) Testing an ORTEC lifetime system. *Materials Science Forum* **666:** 155–159.

Karwasz GP, Zecca A, Brusa RS and Pliszka D (2004) Application of positron annihilation techniques for semiconductor studies. *Journal of Alloys and Compounds* **382:** 244–251.

Leonelli C and Lojkowski W (2007) Main development directions in the application of microwave irradiation to the synthesis of nanopowders. *Chemistry Today* **25:** 34–38.

Lloyd AC (1999) The power plant in your basement. *Scientific American* **281:** 80–86.

Łojkowski W, Millers D, Fidelus J *et al*. (2005) Zirconium dioxide luminescence oxygen sensor. EP 1920238 B1, US 7, 888, 658 B2, EP 1920238 B1, assigned: Instytut Wysokich Cisnien Polskiej Akademii Nauk (Warsaw, PL).

McCormick PG, Tsuzuki T, Robinson JS and Ding J (2001) Nanopowders synthesized by mechanochemical processing. *Advanced Materials* **13:** 1008–1010.

Mercera PDL, van Ommen JG, Doesburg EBM, Burggraaf AJ and Ross JRH (1990) Zirconia as a support for catalysts: Evolution of the texture and structure on calcination in air. *Applied Catalysis A* **57:** 127–148.

Pajonk GM (1991) Aerogel catalysis. *Applied Catalysis A* **72:** 217–266.

Procházka I, Čižek J, Kuriplach J *et al.* (2008) Positron lifetimes in zirconia-based nanomaterials. *Acta Physica Polonica*, **113:** 1495–1499.

Procházka I, Čižek J, Melichova O *et al*. (2011) Positron annihilation study of yttria-stabilized zirconia nanopowders containing Cr2O3 additive. *Journal of Physics: Conference Series* **265:** 1–6.

Ray JC, Pati RK and Pramanik P (2000) Chemical synthesis and structural characterization of nanocrystalline powders of pure zirconia and yttria stabilized zirconia (YSZ). *Journal of the European Ceramic Society* **20:**1289–1295.

Rodríguez-Carvajal J (1993) Recent advances in magnetic structure determination by neutron powder diffraction. *Physica B: Condensed Matter* **192:** 55–69.

Roy R and Komarneni S (1992) Penn State Invention Disclosure No. 92–1110.

Ruiz–Morales JC, Canales–Vázquez J, Savaniu C *et al*. (2006) Disruption of extended defects in solid oxide fuel cell anodes for methane oxidation. *Nature* **439:** 568–571.

Shukla S and Seal S (2005) Mechanisms of room temperature metastable tetragonal phase stabilisation in zirconia. *International Materials Reviews* **50:** 45–64.

Smith DK and Newkirk HW (1965) The crystal structure of baddeleyite (monoclinic ZrO_2) and its relation to the polymorphism of ZrO_2. *Acta Crystallographica* **18:** 983–991.

Smits K, Grigorjeva L, Millers D *et al.* (2011) Intrinsic defect related luminescence in ZrO_2. *Journal of Luminescence* **131:** 2058–2062.

Sõmiya S and Akiba T (1999) Hydrothermal zirconia powders: a bibliography. *Journal of the European Ceramic Society* **19**: 81–87.

Subbarao EG (1981) Zirconia-an overview. In *Advances in Ceramics/Science and Technology of Zirconia* (Heuer AH and Hobbs LW (eds)). Elsevier, Amsterdam, pp 1–24.

Teufer G (1962) Crystal structure of tetragonal ZrO_2. *Acta Crystallographica* **15 :** 1187–1188.

Wyckoff RWG (ed.) (1963) *Crystal Structures*. 2nd edn. Vol. 1. Wiley, New York .

Yang X, Fu J, Jin C *et al.* (2010) Formation mechanism of CaTiO3 hollow crystals with different microstructures. *Journal of the American Chemical Society* **132**: 14279–14287.

Zecca A, Bettonte M, Paridaens J, Karwasz GP and Brusa RS (1998) A new electrostatic positron beam for surface studies. *Measurement Science and Technology* **9:** 409–416.

Zecca A and Karwasz G (2001) Positrons go into detail. *Physics World* **14**: 11, 21–22.

Zhou W, Hunter HMA, Wright PA, Ge Q and Thomas JM (1998) Imaging the pore structure and polytypic intergrowths in mesoporous silica. *Journal of Physics Chemistry* **102**: 6933–6936.

Zhou WZ (2008) Microscopic study of crystal defects enriches our knowledge of materials chemistry. *Journal of Materials Chemistry* **18**: 5321–5325.